arXiv:1906.09957v1 [eess.IV] 21 Jun 2019

Dense three dimensional localization microscopy by deep learning

Elias Nehme[1,2], Daniel Freedman[3], Racheli Gordon[2], Boris Ferdman[2,4], Tomer Michaeli[1], and Yoav Shechtman[2,5,*]

[1]Department of Electrical Engineering, Technion, 32000 Haifa, Israel
[2]Department of Biomedical Engineering, Technion, 32000 Haifa, Israel
[3]Google Research, Haifa, Israel
[4]Russel Berrie Nanotechnology Intitute, Technion, 32000 Haifa, Israel
[5]Lorey Lokey Center for Life Sciences and Engineering, Technion, 32000 Haifa, Israel
[*]Corresponding author: yoavsh@bm.technion.ac.il

Abstract

Localization microscopy is an imaging technique in which the positions of individual nanoscale point emitters (e.g. fluorescent molecules) are determined at high precision from their images. This is the key ingredient in single/multiple-particle-tracking [1, 2] and several super-resolution microscopy approaches [3–5]. Localization in three-dimensions (3D) can be performed by modifying the image that a point-source creates on the camera, namely, the point-spread function (PSF), using additional optical elements [6]. However, localizing multiple adjacent emitters in 3D poses a significant algorithmic challenge, due to the lateral overlap of their PSFs. Here, we train a neural net to receive an image containing densely overlapping PSFs of multiple emitters over a large axial range, and output a list of their 3D positions. Furthermore, we then use the net to design the optimal PSF for the multi-emitter case. We demonstrate our approach numerically as well as experimentally by volumetrically imaging dozens of fluorescently-labeled telomeres occupying a mammalian nucleus in a single snapshot.

1 Introduction

Determining the microscopic position of a point emitter imaged with an optical microscope is at the heart of modern imaging techniques such as single particle tracking [1] and super-resolution localization microscopy, namely, photoactivated localization microscopy [(F)PALM] [3, 4], and stochastic optical reconstruction microscopy (STORM) [5]. These techniques have revolutionized biological imaging in the last decade, enabling the observation of cellular processes and structures at the nanoscale [7].

In order to enable the imaging of three-dimensional (3D) objects, microscopic particle localization has been extended to 3D via various methods [6], a prominent one being point spread function (PSF) engineering [8–10]. In PSF engineering, the image that a point source creates on the detector plane, namely, the PSF, is modified by additional optical elements, e.g. a phase mask, inserted into the detection path of a standard microscope [11] (Fig. 1a). This enables the encoding of the axial position of an emitter in the PSF, where it can be recovered via image processing using a theoretical or experimentally-calibrated PSF model [10, 12–14]. The phase-mask pattern uniquely determines the shape of the PSF.

In many applications it is desired to image multiple, nearby emitters in 3D. In localization microscopy, for example, the num-

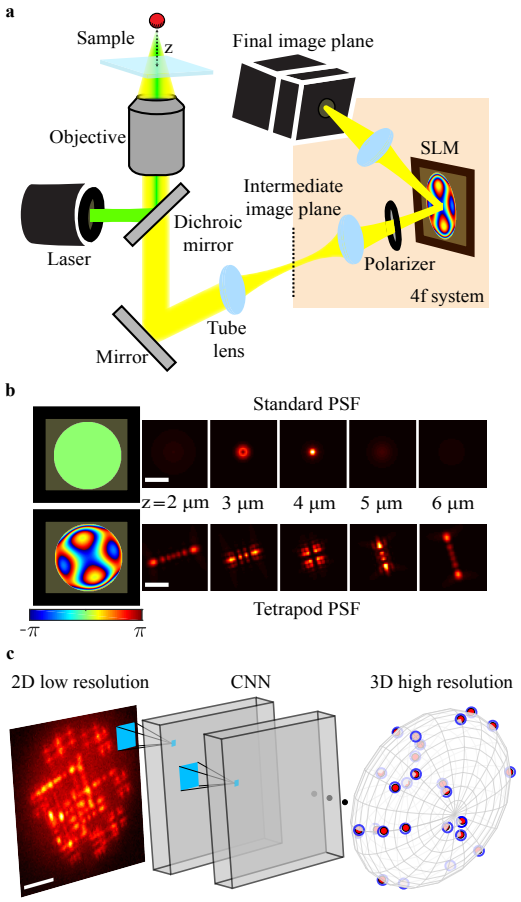


Fig. 1. Optical setup and approach overview. **a** The light emitted from a fluorescent microscopic particle is collected by the objective and focused through the tube lens into an image at the intermediate image-plane. This plane is extended using a 4f system with an SLM placed at the Fourier plane in between the 2 4f lenses. **b** The phase mask implemented on the SLM dictates the PSF's axial profile measured on the final image plane. **c** After training, our CNN receives a 2D low resolution image of overlapping Tetrapod PSFs and outputs a 3D high-resolution volume which is translated to a list of 3D localizations. Blue empty spheres denote simulated GT positions along the surface of an ellipsoid. Red spheres denote CNN detections. Scale bar is 3 μm.

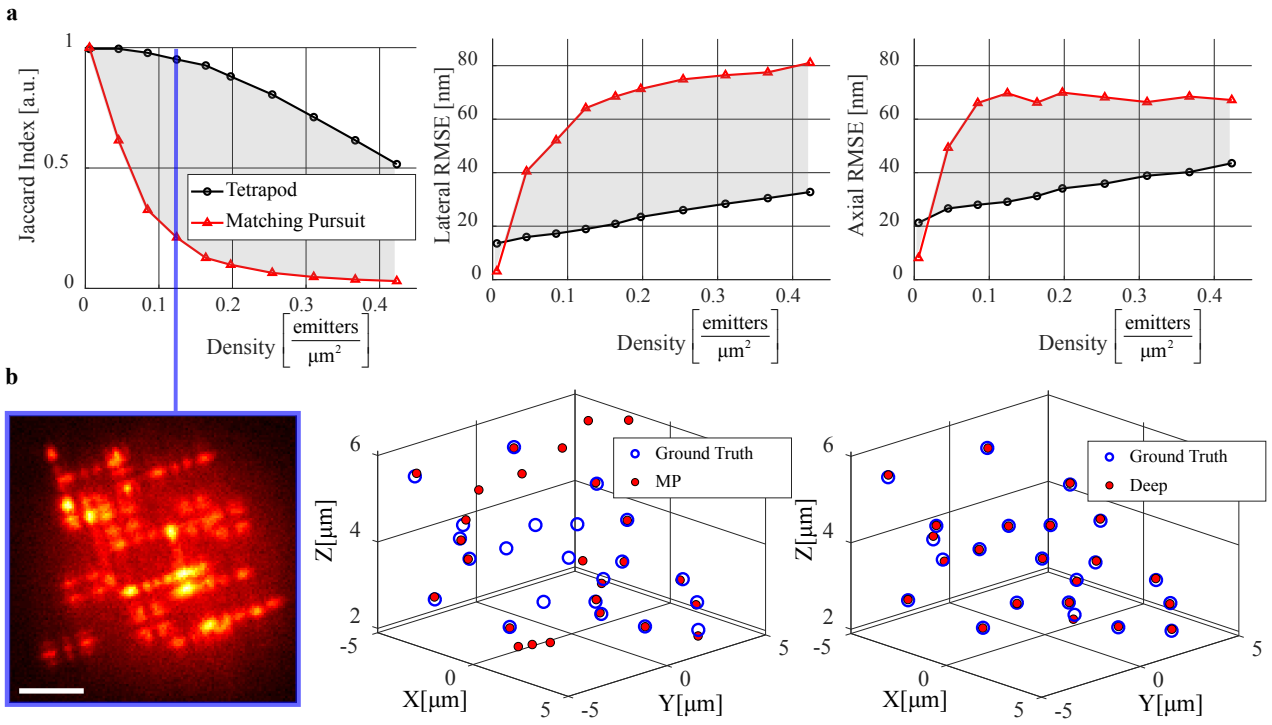


Fig. 2. Comparison to MP. **a** The trained CNN is superior to the matching pursuit approach in both detectability (Jaccard index) and in accuracy (Lateral \Axial RMSE). Matching of points was computed with a threshold distance of 150 nm using the Hungarian algorithm [15]. **b** Example of a simulated frame of density 0.124 $\left[\frac{\text{emitters}}{\mu m^2}\right]$ alongside 3D comparisons of the recovered positions by MP (middle) and by the CNN (right). Scale bar is 2 μm.

ber of emitters per frame (and thereby their density) determines the temporal resolution of the method. Alternatively, when tracking multiple sub-cellular elements, those may be co-located with close proximity, such that the shapes of their PSFs overlap. However, regions with a high density of overlapping emitters pose a severe algorithmic challenge even in 2D localization, and much more so in the 3D case; encoding the axial position of an emitter introduces additional complexity into the PSF shape and increases its size, especially for large axial ranges (>3 μm) using the Tetrapod PSF [10, 16] (Fig. 1 b). Consequently, while for the in-focus standard PSF case, a variety of methods have been developed to cope with overlapping emitters [17–19], the current achievable performance in 3D high-density localization is far from satisfactory [20].

Recently, deep learning has proven to be a useful tool for microscopic data analysis [21–26], and specifically for localization microscopy [19, 27–33]. Moreover, an emerging promising application of deep learning is to jointly design the optical system alongside the data processing algorithm, enabling end-to-end optimization of both components [34–42].

Here we present two fundamental contributions to tackle the problem of high-density overlapping PSFs in 3D localization. First, we employ a convolutional neural network (CNN) for 3D localization from dense fields of overlapping emitters with engineered PSFs, and demonstrate it using the Tetrapod PSF [10, 16]. Second, we design an optimal PSF for high-density 3D microscopic particle localization for a large axial range of 4 μm. This is done by incorporating a physical-simulation layer in the CNN with an adjustable phase modulation, thus jointly learning the reconstruction (decoding) and the optimal PSF (encoding). Our approach is highly flexible and can be easily adapted to any 3D localization data set. We validate our approach on both simulated and experimental data, demonstrating for the first time robust and precise localization of a high density of emitters in 3D.

2 Results

The optimal engineered-PSF for encoding the 3D position of a single point emitter, derived by maximizing the Fisher Information of the system [43] is the Tetrapod PSF [10, 16]. The Tetrapod PSF offers an extremely large axial localization range (up to 20 μm [16]), however, its large lateral footprint poses a major challenge for dense 3D localization of microscopic particles; currently, there is no method capable of localization of dense emitters over a large axial range [20]. While recent work has addressed single emitter and dense 3D localization by CNN [27, 29, 31], dense emitter localization over a large axial range (>2 μm) has not been demonstrated to date, neither experimentally nor in simulation.

To solve the high-density localization problem in 3D, we trained a CNN that receives a 2D image of overlapping Tetrapod PSFs spanning an axial range of 4 μm, and outputs a 3D grid with a voxel-size of $27.5 \times 27.5 \times 50\ nm^3$ (Fig. 1c). For architecture details and learning hyper-parameters see Supplementary Information. To compile a list of localizations, we apply simple post-processing on the output 3D grid by clustering nearby detections into connected components, thresholding, and local maximum finding (Supplementary Information section 3.4).

We compare our method to a fit-and-subtract based Match-

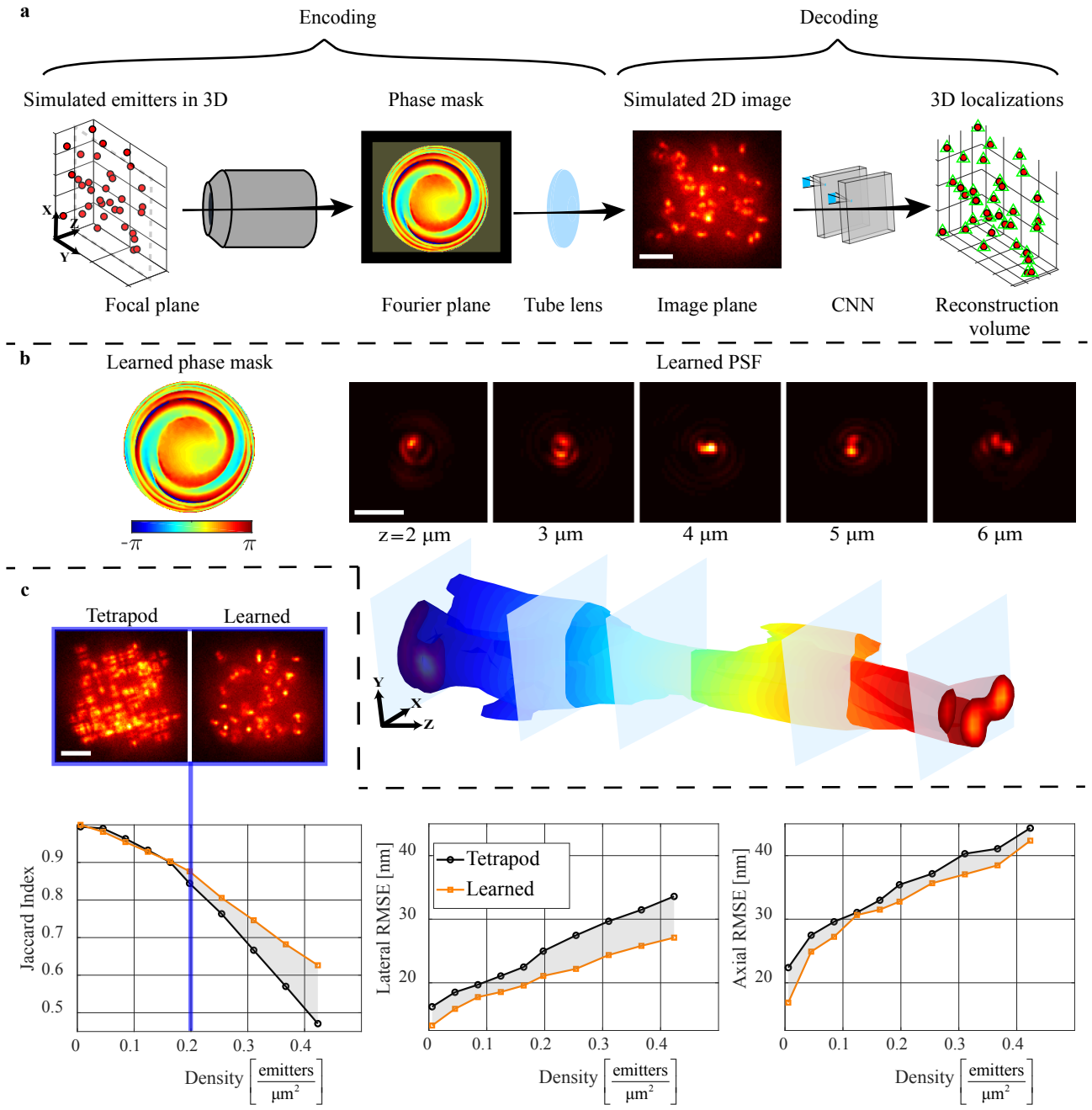


Fig. 3. PSF Learning. **a** Simulated 3D emitter positions are fed to the image formation model to simulate their low resolution CCD image (Encoding). Next, this image is fed to a CNN that tries to recover the simulated emitter positions (Decoding). The difference between the simulated positions and the positions recovered by the CNN is used to jointly optimize the phase mask at the Fourier plane, and the recovery CNN parameters. **b** Learned phase mask (left), with a simulation of the learned PSF as function of the emitter axial position (right). 3D isosurface rendering of the learned PSF (bottom). **c** Example frame of density 0.197 $\left[\frac{\text{emitters}}{\mu m^2}\right]$ (top) with the same simulated emitter positions, using the Tetrapod (left) and the learned PSF (right). Jaccard index and lateral \axial RMSE comparison (bottom) between two CNNs with the same architecture, one trained to recover 3D positions from 2D images of Tetrapod PSF (black), and the second trained to recover 3D positions from 2D images of the learned PSF (orange). Scale bar is 3 μm.

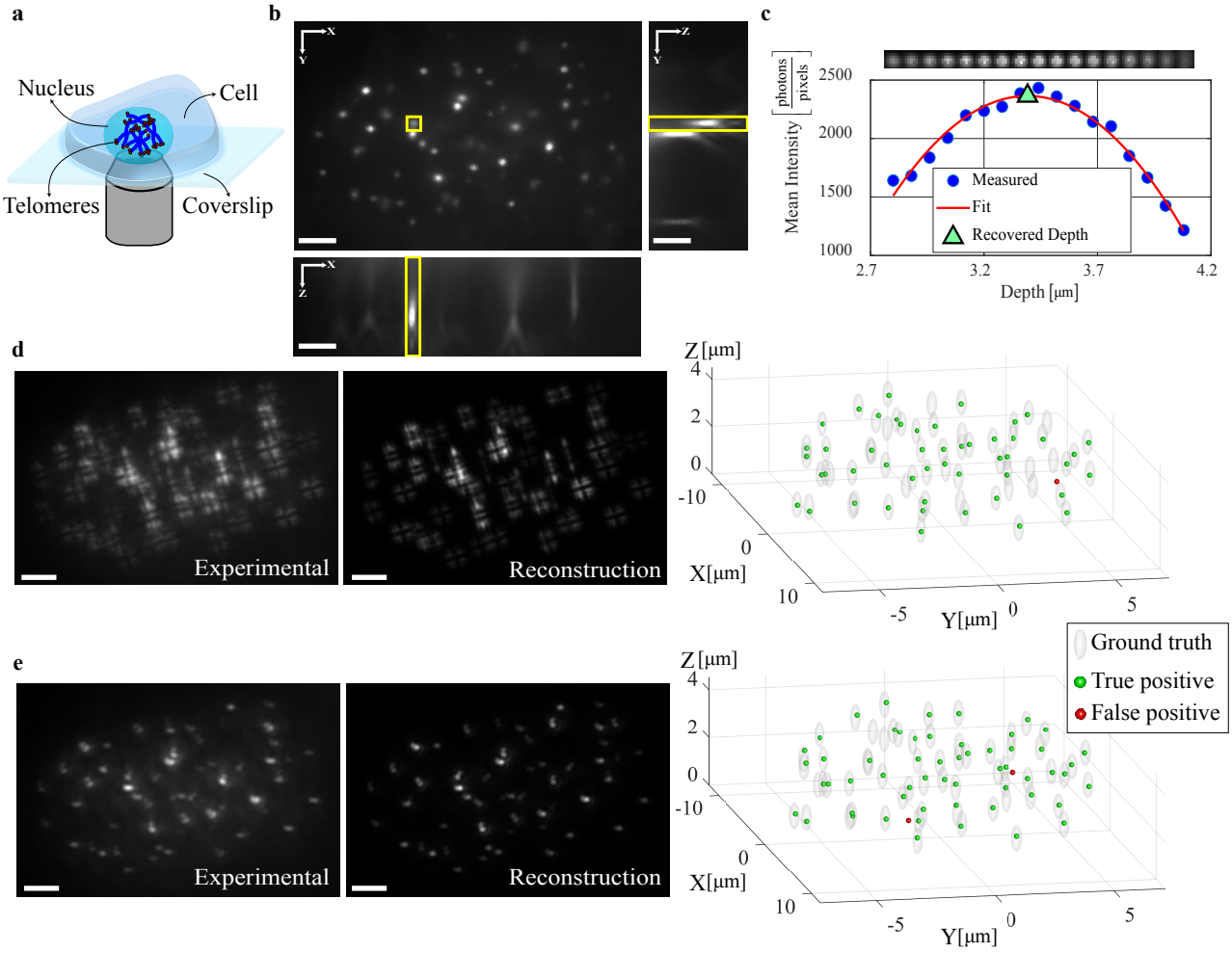


Fig. 4. Experimental demonstration. **a** Schematic of imaging fixed U2OS cells with fluorescent labeled telomeres inside their nucleus. **b** Focus slice with the standard PSF inside a U2OS cell nucleus, obtained via a z-scan. The yellow rectangles mark the same emitter in all three orthogonal planes. **c** Example fit of the mean intensity in sequential axial slices used to estimate the approximate emitter axial position. **d** Experimental snapshot with the Tetrapod PSF (left), rendered image from the 3D recovered positions by the Tetrapod CNN (middle), and a 3D comparison of the recovered positions and the approximate experimental ground truth (right). **e** Experimental snapshot with the learned PSF (left), rendered image from the 3D recovered positions by the learned PSF CNN (middle), and a 3D comparison of the recovered positions and the approximate experimental ground truth (right). Scale bar is 3 μm.

ing Pursuit (MP) approach [44] (see Supplementary Information section 4) as currently there is no other method capable of localizing overlapping Tetrapod PSFs. To quantitatively compare our method with MP, we simulated 100 images per density for 10 different densities in the range of 1-75 emitters per field-of-view of $13 \times 13\ \mu m^2$, with a mean signal of 30K $\left[\frac{photons}{emitter}\right]$ and a mean background of 150 $\left[\frac{photons}{pixel}\right]$. The results are shown in Fig. 2. As evident in both the Jaccard index (defined as $\frac{TP}{TP+FP+FN}$, where TP, FP, FN are true positives, false positives, and false negatives [20]) and the lateral/axial RMSE (Fig. 2a) the CNN achieves remarkable performance in localizing high-density Tetrapods.

Not surprisingly, for the single-emitter case, the RMSE of the MP localization is lower (better) than that of the CNN. This is because for a single-emitter, MP is equivalent to a continuous Maximum Likelihood Estimator (MLE) (Supplementary Information section 4), which is asymptotically optimal [45], whereas the CNN's precision is bounded by pixelization of the grid (i.e. half voxel of 13.75 nm in xy and 25 nm in z). However, quickly beyond the single-emitter case, the CNN drastically outperforms MP. A similar result was obtained when compared to a leading single-emitter fitting method [14] applicable also for the multiple emitter case [20] (see Supplementary Information section 6).

The Tetrapod PSF was optimized for the single emitter case [10, 16]. However, when considering the multiple-emitter case, an intriguing question arises: What is the optimal PSF for high density 3D localization over a large axial range? And in what sense is it optimal? To answer this question we need to rethink the design metric; extending the Fisher Information criterion [10] to account for emitter density is not-trivial, and while it is intuitive that a smaller-footprint PSF would be preferable for dense emitters, it is not clear how to mathematically balance this demand with the requirement for high localization precision per emitter.

Our PSF-design logic is based on the following: since we have already established that a CNN yields superior reconstruction for high-density 3D localization, *we are interested in a PSF (encoder) that would be optimally localized by a CNN (decoder)*. Therefore, in contrast to a sequential paradigm where the PSF and the localization algorithm are optimized separately, we adopt a co-design approach (Fig. 3 a). To jointly optimize the PSF and the localization CNN, we introduce a differentiable physical simulation layer, which is parametrized by a phase mask that dictates the microscope's PSF. This layer encodes 3D point sources to their respective low-resolution 2D image (see Supplementary Information section 2). Then, this image is fed to the localization CNN which decodes it and recovers the underlying 3D source positions. During training, the net is presented with simulated point sources at random locations and, using the difference between the CNN recovery and the simulated 3D positions we optimize both the phase mask and the localization CNN parameters in an end-to-end fashion. The learned PSF (Fig. 3 b) has a small lateral footprint, which is critical for minimizing overlaps at high densities. Moreover, the learned phase mask twists in a spiral trajectory causing the PSF to rapidly rotate throughout the axial range, a trait that was previously shown to be valuable for encoding depth [8].

To quantify the improvement introduced by our new PSF, we first compare it to the Tetrapod PSF in simulations. Specifically, we train a similar reconstruction net for both the Tetrapod and the learned PSF using a matching training set composed of simulated continuous 3D positions along with their corresponding 2D low-resolution images. The learned PSF performs similar to the Tetrapod PSF for low emitter densities (Fig. 3 c). However, as the density goes up the learned PSF outperforms the Tetrapod PSF in both localization accuracy and in emitter detectability (Jaccard index) (Fig. 3 c). This result is not surprising, as the learned PSF has a smaller spatial foorprint, and hence it is less likely to overlap than the Tetrapod (Fig. 3 c). Importantly, we see that this boost in the Jaccard index does not come at a cost of precision (lateral/axial RMSE), which is crucial, as we would like to maintain high localization precision under high emitter-density.

Next, we demonstrate the applicability of our method experimentally by imaging fixed U2OS cells with fluorescently labeled telomeres (TRF1-DsRed) [46]. The cell contains tens of telomeres squeezed in the volume of a nucleus with ≈ 20 μm diameter (Fig. 4 a, b). From a single snapshot focused inside the nucleus, the CNN outputs a list of 3D positions of telomeres spanning an axial range of ≈ 3 μm. Using the Tetrapod PSF snapshot, the Tetrapod-trained CNN was able to recover 49 out of 62 telomeres with a single false positive, yielding a Jaccard index of 0.77 (Fig. 4 d). In comparison, using the learned PSF snapshot, the corresponding CNN was able to recover 57 out of the 62 telomeres with only 2 false positives, yielding a Jaccard index of 0.89 (Fig. 4 e). The recovered positions were compared to approximated ground-truth 3D positions (Fig. 4 c), obtained by axial scanning and 3D fitting (see Supplementary Information section 8).

To qualitatively compare the recovered list of localizations to the acquired snapshot, we fed this list to the physical simulation layer and generated the matching 2D low-resolution image (Fig. 4 d,e). As verified by the re-generated images, the 3D positions of the telomeres are faithfully recovered by the CNNs. Moreover, the misses in both snapshots were either due to local unaccounted for aberrations and/or an extremely low number of signal photons (see Supplementary Information for more experimental results).

3 Discussion

To conclude, in this work we demonstrated for the first time, numerically and experimentally in cells, 3D localization of dense emitters over a large axial range. Moreover, our proposed approach is highly flexible and is easily adapted to experimental challenges, e.g. experimental PSF aberrations, as demonstrated in the presented telomere images. Finally, we proposed a novel approach to jointly engineer the PSF of a microscope alongside the localization algorithm. The presented co-design approach may pave the way to a wide variety of interesting applications in the field of microscopy where the optics were traditionally designed separately from the image processing algorithm that follows.

Notably, the phase mask was optimized over a large subspace (pixelwise), rather than over a small subspace, e.g. Zernike polynomials [10]. Increasing this optimization space naturally enables more flexibility and potentially improved results. Importantly, the ability to train the net solely on simulated data and apply the resulting model to experimental data with similar conditions (as previously demonstrated [19]) was crucial for the method to work; it also emphasizes an inherent advantage of neural nets over most existing localization methods: tremendous flexibility to cope with a variety of observed challenges, e.g. spatially-varying background and variable emitter size (see Supplementary Information section 3.1).

Our work triggers many possible questions and research directions regarding its capabilities and limitations. For example, how globally-optimal is the resulting PSF? Similarly, how sensitive is the resulting PSF and its performance to different loss functions, CNN architectures, initializations (e.g. with an existing phase mask), and the sampled training set of locations? Currently, it is unclear how each of these components affects the learning process. For example, it may be beneficial to apply a biased sampling scheme throughout training, i.e. to include in the training data more emitters towards the edges of the axial range.

Funding Information

Google; H2020 European Research Council Horizon 2020 (802567); Israel Academy of Sciences and Humanities (Alon Fellowship Program); Israel Science Foundation (ISF) (852/17); Ollendorff Foundation; Technion-Israel Institute of Technology (Career Advancement Chairship); Zuckerman Foundation.

Acknowledgements

The authors wish to thank the Garini lab for the U2OS cells. We also thank Jonas Ries for his help with the application of SMAP-2018 to Tetrapod PSFs. We gratefully acknowledge the support of NVIDIA Corporation with the donation of the Titan V GPU used for this research. Finally, we thank Google for the research cloud units provided to accelerate this research.

References

[1] Y. Katayama, O. Burkacky, M. Meyer, C. Bräuchle, E. Gratton, and D. C. Lamb, "Real-time nanomicroscopy via three-dimensional single-particle tracking," *ChemPhysChem*, vol. 10, no. 14, pp. 2458–2464, 2009.

[2] C. Manzo and M. F. Garcia-Parajo, "A review of progress in single particle tracking: from methods to biophysical insights," *Reports on progress in physics*, vol. 78, no. 12, p. 124601, 2015.

[3] E. Betzig, G. H. Patterson, R. Sougrat, O. W. Lindwasser, S. Olenych, J. S. Bonifacino, M. W. Davidson, J. Lippincott-Schwartz, and H. F. Hess, "Imaging intracellular fluorescent proteins at nanometer resolution," *Science*, 2006.

[4] S. T. Hess, T. P. Girirajan, and M. D. Mason, "Ultra-high resolution imaging by fluorescence photoactivation localization microscopy," *Biophysical Journal*, vol. 91, no. 11, pp. 4258 – 4272, 2006.

[5] M. J. Rust, M. Bates, and X. Zhuang, "Sub-diffraction-limit imaging by stochastic optical reconstruction microscopy (STORM)," *Nature Methods*, vol. 3, no. 10, pp. 793–795, 2006.

[6] A. von Diezmann, Y. Shechtman, and W. Moerner, "Three-dimensional localization of single molecules for super-resolution imaging and single-particle tracking," *Chemical reviews*, vol. 117, no. 11, pp. 7244–7275, 2017.

[7] S. J. Sahl and W. Moerner, "Super-resolution fluorescence imaging with single molecules," *Current Opinion in Structural Biology*, vol. 23, no. 5, pp. 778 – 787, 2013.

[8] S. R. P. Pavani, M. A. Thompson, J. S. Biteen, S. J. Lord, N. Liu, R. J. Twieg, R. Piestun, and W. Moerner, "Three-dimensional, single-molecule fluorescence imaging beyond the diffraction limit by using a double-helix point spread function," *Proceedings of the National Academy of Sciences*, vol. 106, no. 9, pp. 2995–2999, 2009.

[9] B. Huang, W. Wang, M. Bates, and X. Zhuang, "Three-dimensional super-resolution imaging by stochastic optical reconstruction microscopy," *Science*, vol. 319, no. 5864, pp. 810–813, 2008.

[10] Y. Shechtman, S. J. Sahl, A. S. Backer, and W. Moerner, "Optimal point spread function design for 3d imaging," *Physical review letters*, vol. 113, no. 13, p. 133902, 2014.

[11] A. S. Backer and W. Moerner, "Extending single-molecule microscopy using optical fourier processing," *The Journal of Physical Chemistry B*, vol. 118, no. 28, pp. 8313–8329, 2014.

[12] S. Liu, E. B. Kromann, W. D. Krueger, J. Bewersdorf, and K. A. Lidke, "Three dimensional single molecule localization using a phase retrieved pupil function," *Optics express*, vol. 21, no. 24, pp. 29462–29487, 2013.

[13] H. P. Babcock and X. Zhuang, "Analyzing single molecule localization microscopy data using cubic splines," *Scientific reports*, vol. 7, no. 1, p. 552, 2017.

[14] Y. Li, M. Mund, P. Hoess, J. Deschamps, U. Matti, B. Nijmeijer, V. J. Sabinina, J. Ellenberg, I. Schoen, and J. Ries, "Real-time 3d single-molecule localization using experimental point spread functions," *Nature methods*, vol. 15, no. 5, p. 367, 2018.

[15] H. W. Kuhn, "The hungarian method for the assignment problem," *Naval research logistics quarterly*, vol. 2, no. 1-2, pp. 83–97, 1955.

[16] Y. Shechtman, L. E. Weiss, A. S. Backer, S. J. Sahl, and W. Moerner, "Precise three-dimensional scan-free multiple-particle tracking over large axial ranges with tetrapod point spread functions," *Nano letters*, vol. 15, no. 6, pp. 4194–4199, 2015.

[17] J. Min, C. Vonesch, H. Kirshner, L. Carlini, N. Olivier, S. Holden, S. Manley, J. C. Ye, and M. Unser, "Falcon: fast and unbiased reconstruction of high-density super-resolution microscopy data," *Scientific reports*, vol. 4, p. 4577, 2014.

[18] N. Boyd, G. Schiebinger, and B. Recht, "The alternating descent conditional gradient method for sparse inverse problems," *SIAM Journal on Optimization*, vol. 27, no. 2, pp. 616–639, 2017.

[19] E. Nehme, L. E. Weiss, T. Michaeli, and Y. Shechtman, "Deep-storm: super-resolution single-molecule microscopy by deep learning," *Optica*, vol. 5, no. 4, pp. 458–464, 2018.

[20] D. Sage, T.-A. Pham, H. Babcock, T. Lukes, T. Pengo, J. Chao, R. Velmurugan, A. Herbert, A. Agrawal, S. Colabrese, *et al.*, "Super-resolution fight club: assessment of 2d and 3d single-molecule localization microscopy software," *Nature methods*, vol. 16, no. 5, p. 387, 2019.

[21] Y. Rivenson, Y. Zhang, H. Günaydın, D. Teng, and A. Ozcan, "Phase recovery and holographic image reconstruction using deep learning in neural networks," *Light: Science & Applications*, vol. 7, no. 2, p. 17141, 2018.

[22] T. Nguyen, Y. Xue, Y. Li, L. Tian, and G. Nehmetallah, "Deep learning approach for fourier ptychography microscopy," *Optics express*, vol. 26, no. 20, pp. 26470–26484, 2018.

[23] M. Weigert, U. Schmidt, T. Boothe, A. Müller, A. Dibrov, A. Jain, B. Wilhelm, D. Schmidt, C. Broaddus, S. Culley, *et al.*, "Content-aware image restoration: pushing the limits of fluorescence microscopy," *Nature methods*, vol. 15, no. 12, p. 1090, 2018.

[24] Y. Rivenson, T. Liu, Z. Wei, Y. Zhang, K. de Haan, and A. Ozcan, "Phasestain: the digital staining of label-free quantitative phase microscopy images using deep learning," *Light: Science & Applications*, vol. 8, no. 1, p. 23, 2019.

[25] T. Liu, K. de Haan, Y. Rivenson, Z. Wei, X. Zeng, Y. Zhang, and A. Ozcan, "Deep learning-based super-resolution in coherent imaging systems," *Scientific reports*, vol. 9, no. 1, p. 3926, 2019.

[26] J. T. Smith, R. Yao, N. Sinsuebphon, A. Rudkouskaya, J. Mazurkiewicz, M. Barroso, P. Yan, and X. Intes, "Ultra-fast fit-free analysis of complex fluorescence lifetime imaging via deep learning," *bioRxiv*, p. 523928, 2019.

[27] N. Boyd, E. Jonas, H. P. Babcock, and B. Recht, "Deeploco: Fast 3d localization microscopy using neural networks," *BioRxiv*, p. 267096, 2018.

[28] W. Ouyang, A. Aristov, M. Lelek, X. Hao, and C. Zimmer, "Deep learning massively accelerates super-resolution localization microscopy," *Nature biotechnology*, 2018.

[29] P. Zhang, S. Liu, A. Chaurasia, D. Ma, M. J. Mlodzianoski, E. Culurciello, and F. Huang, "Analyzing complex single-molecule emission patterns with deep learning," *Nature methods*, vol. 15, no. 11, p. 913, 2018.

[30] J. M. Newby, A. M. Schaefer, P. T. Lee, M. G. Forest, and S. K. Lai, "Convolutional neural networks automate detection for tracking of submicron-scale particles in 2d and 3d," *Proceedings of the National Academy of Sciences*, vol. 115, no. 36, pp. 9026–9031, 2018.

[31] P. Zelger, K. Kaser, B. Rossboth, L. Velas, G. Schütz, and A. Jesacher, "Three-dimensional localization microscopy using deep learning," *Optics express*, vol. 26, no. 25, pp. 33166–33179, 2018.

[32] K. Liu, H. Qiao, J. Wu, H. Wang, L. Fang, and Q. Dai, "Fast 3d cell tracking with wide-field fluorescence microscopy through deep learning," *arXiv preprint arXiv:1805.05139*, 2018.

[33] B. Diederich, P. Then, A. Jügler, R. Förster, and R. Heintzmann, "cellstorm—cost-effective super-resolution on a cellphone using dstorm," *PloS one*, vol. 14, no. 1, p. e0209827,

2019.
[34] A. Chakrabarti, "Learning sensor multiplexing design through back-propagation," in *Advances in Neural Information Processing Systems*, pp. 3081–3089, 2016.
[35] R. Horstmeyer, R. Y. Chen, B. Kappes, and B. Judkewitz, "Convolutional neural networks that teach microscopes how to image," *arXiv preprint arXiv:1709.07223*, 2017.
[36] A. Turpin, I. Vishniakou, and J. D. Seelig, "Light scattering control with neural networks in transmission and reflection," *arXiv preprint arXiv:1805.05602*, 2018.
[37] H. Haim, S. Elmalem, R. Giryes, A. M. Bronstein, and E. Marom, "Depth estimation from a single image using deep learned phase coded mask," *IEEE Transactions on Computational Imaging*, vol. 4, no. 3, pp. 298–310, 2018.
[38] L. He, G. Wang, and Z. Hu, "Learning depth from single images with deep neural network embedding focal length," *IEEE Transactions on Image Processing*, vol. 27, no. 9, pp. 4676–4689, 2018.
[39] E. Hershko, L. E. Weiss, T. Michaeli, and Y. Shechtman, "Multicolor localization microscopy and point-spread-function engineering by deep learning," *Optics express*, vol. 27, no. 5, pp. 6158–6183, 2019.
[40] V. Sitzmann, S. Diamond, Y. Peng, X. Dun, S. Boyd, W. Heidrich, F. Heide, and G. Wetzstein, "End-to-end optimization of optics and image processing for achromatic extended depth of field and super-resolution imaging," *ACM Transactions on Graphics (TOG)*, vol. 37, no. 4, p. 114, 2018.
[41] J. Chang and G. Wetzstein, "Deep optics for monocular depth estimation and 3d object detection," *arXiv preprint arXiv:1904.08601*, 2019.
[42] Y. Wu, V. Boominathan, H. Chen, A. Sankaranarayanan, and A. Veeraraghavan, "Phasecam3d—learning phase masks for passive single view depth estimation,"
[43] S. M. Kay, *Fundamentals of statistical signal processing*. Prentice Hall PTR, 1993.
[44] Y. Shechtman, L. E. Weiss, A. S. Backer, M. Y. Lee, and W. Moerner, "Multicolour localization microscopy by point-spread-function engineering," *Nature photonics*, vol. 10, no. 9, p. 590, 2016.
[45] P. J. Bickel and K. A. Doksum, *Mathematical Statistics: Basic Ideas and Selected Topics, Volumes I-II Package*. Chapman and Hall/CRC, 2015.
[46] I. Bronshtein, E. Kepten, I. Kanter, S. Berezin, M. Lindner, A. B. Redwood, S. Mai, S. Gonzalo, R. Foisner, Y. Shav-Tal, *et al.*, "Loss of lamin a function increases chromatin dynamics in the nuclear interior," *Nature communications*, vol. 6, p. 8044, 2015.